

Robust 3D gravity gradient inversion by planting anomalous densities

Leonardo Uieda¹ and Valéria C. F. Barbosa¹

ABSTRACT

We have developed a new gravity gradient inversion method for estimating a 3D density-contrast distribution defined on a grid of rectangular prisms. Our method consists of an iterative algorithm that does not require the solution of an equation system. Instead, the solution grows systematically around user-specified prismatic elements, called “seeds,” with given density contrasts. Each seed can be assigned a different density-contrast value, allowing the interpretation of multiple sources with different density contrasts and that produce interfering signals. In real world scenarios, some sources might not be targeted for the interpretation. Thus, we developed a robust procedure that neither requires the isolation of the signal of the targeted sources prior to the inversion nor requires substantial prior information about the nontargeted sources. In our iterative algorithm, the

estimated sources grow by the accretion of prisms in the periphery of the current estimate. In addition, only the columns of the sensitivity matrix corresponding to the prisms in the periphery of the current estimate are needed for the computations. Therefore, the individual columns of the sensitivity matrix can be calculated on demand and deleted after an accretion takes place, greatly reducing the demand for computer memory and processing time. Tests on synthetic data show the ability of our method to correctly recover the geometry of the targeted sources, even when interfering signals produced by nontargeted sources are present. Inverting the data from an airborne gravity gradiometry survey flown over the iron ore province of Quadrilátero Ferrífero, southeastern Brazil, we estimated a compact iron ore body that is in agreement with geologic information and previous interpretations.

INTRODUCTION

Historically, the vertical component of the gravity field has been widely used in exploration geophysics due to the simplicity of its measurement and interpretation. This fact propelled the development of a large variety of gravity inversion methods. Conversely, the technological difficulties in the acquisition of accurate airborne gravity gradiometry data resulted in a delay in the development of methods for the inversion of this kind of data. Consequently, before the early 1990s, few papers published in the literature were devoted to the interpretation (or analysis) of gravity gradiometer data. At this point, two papers deserve the general readers' attention. The first one is [Vasco \(1989\)](#) which presents a comparative study of the vertical component of gravity and the gravity gradient tensor by analyzing their parameter resolution and variance matrices. The second paper is [Pedersen and Rasmussen \(1990\)](#) which studied data of gravity and magnetic gradient tensors and introduced scalar invariants that indicate the dimensionality of the sources.

Recent technological developments of moving-platform gravity gradiometers made it feasible to accurately measure the five linearly independent components of the gravity gradient tensor. These technological advances, paired with the advent of global positioning systems (GPS), have opened a new era in the acquisition of accurate airborne gravity gradiometry data. Thus, airborne gravity gradiometry has come to be a useful tool for interpreting geologic bodies present in mining and hydrocarbon exploration areas. Gravity gradiometry has the advantage, compared with other gravity methods, of being extremely sensitive to localized density contrasts within regional geologic settings ([Zhdanov et al., 2010b](#)).

Recently, some gravity gradient inversion algorithms have been adapted to predominantly interpret both orebodies that are important mineral exploration targets (e.g., [Li, 2001](#); [Zhdanov et al., 2004](#); [Martinez et al., 2010](#); [Wilson et al., 2011](#)), and salt bodies in a sedimentary setting (e.g., [Jorgensen and Kisabeth, 2000](#); [Routh et al., 2001](#)). All these methods discretize the earth's subsurface into prismatic cells with homogeneous density contrasts and

Manuscript received by the Editor 3 October 2011; revised manuscript received 12 April 2012; published online 22 June 2012.

¹Observatório Nacional, Geophysics Department, Rio de Janeiro, Brazil. E-mail: leouieda@gmail.com; valcris@on.br.

© 2012 Society of Exploration Geophysicists. All rights reserved.

estimate a 3D density-contrast distribution, thus retrieving an image of geologic bodies. Usually, a gravity gradient data set contains a huge volume of observations of the five linearly independent tensor components. These observations are collected every few meters in surveys that may contain hundreds to thousands of line kilometers. This massive data set combined with the discretization of the earth's subsurface into a fine grid of prisms results in a large-scale 3D inversion with hundreds of thousands of parameters and tens of thousands of data.

The solution of a large-scale 3D inversion requires overcoming two main obstacles. The first one is the large amount of computer memory required to store the matrices used in the computations, particularly the sensitivity matrix. The second obstacle is the computational time required for matrix-vector multiplications and to solve the resulting linear system. One approach to overcome these problems is to use the fast Fourier transform for matrix-vector multiplications by exploiting the translational invariance of the kernels to reduce the linear operators to Toeplitz block structure (Pilkington, 1997; Zhdanov et al., 2004; Wilson et al., 2011). However, these approaches are unable to deal with data on an irregular grid or on an uneven surface. Furthermore, the observations must lie above the surface topography, so these approaches cannot be applied to borehole data. Another strategy for the solution of large-scale 3D inversions involves using a variety of data compression techniques. Portniaguine and Zhdanov (2002) use a compression technique based on cubic interpolation. Li and Oldenburg (2003) use a 3D wavelet compression on each row of the sensitivity matrix. Most recently, an alternative strategy for the solution of large-scale 3D inversion has been used under the name of "moving footprint" (Cox et al., 2010; Zhdanov et al., 2010a; Wilson et al., 2011). In this approach the full sensitivity matrix is not computed; rather, for each row, only the few elements that lie within the radius of the footprint size are calculated. In other words, the j th element of the i th row of sensitivity matrix only needs to be computed if its distance from the i th observation is smaller than a prespecified footprint size (expressed in kilometers). The footprint size is a threshold value defined by the user and will depend on the natural decay of the Green's function for the gravity field. The smaller the footprint size, the larger the number of null elements in the rows of the sensitivity matrix; hence, the faster the inversion will be but also the greater is the loss of accuracy. The user can then either accept the result or increase the footprint size and restart the inversion. This procedure leads to a sparse representation of the sensitivity matrix allowing the solution of intractable large-scale 3D inversions via the conjugate gradient technique.

Depending on the regularization function used, inversion methods for estimating a 3D density-contrast distribution that discretize the earth's subsurface into prismatic cells can produce either blurred images (e.g., Li and Oldenburg, 1998) or sharp images of the anomalous sources (e.g., Portniaguine and Zhdanov, 1999; Zhdanov et al., 2004; Silva Dias et al., 2009, 2011). Nevertheless, all of the above-mentioned methods require the solution of a large linear system, which is, as pointed out before, one of the biggest computational hurdles for large-scale 3D inversions. Alternatively, there is a class of gravity inversion methods that do not solve linear systems but instead search the space of possible solutions for an optimum one. This class can be further divided into methods that use random search and those that use systematic search algorithms. Among the methods that use random search, we draw attention to the

two following methods. Nagihara and Hall (2001) estimate a 3D density-contrast distribution using the simulated annealing algorithm (SA). Krahenbuhl and Li (2009) retrieve a salt body subject to density contrast constraints by developing a hybrid algorithm that combines the genetic algorithm (GA) with a modified form of SA as well as a local search technique that is not activated at every generation of the GA. On the other hand, examples of methods that use a systematic search are the methods of Zidarov and Zhelev (1970), Camacho et al. (2000), and René (1986). Zidarov and Zhelev's (1970) bubbling method looks for a compact source solution (without hollows in its interior) by transforming a given initial nonnull spatially discrete density-contrast distribution ρ inside a region \mathfrak{R} into a constant distribution $\rho^* \leq \rho$ inside a region $\mathfrak{R}^* \supset \mathfrak{R}$ by successive redistribution of the excess of mass of ρ relative to ρ^* in outward directions. Both distributions fit the gravity data. To overcome the difficulty of setting an initial density-contrast distribution ρ that not only fits the data, but also satisfies the constraint that ρ be everywhere greater than or equal to a specified upper bound, Cordell (1994) adapts the bubbling method starting with point mass estimates obtained via Euler's homogeneity equation. Following the class of systematic search methods, Camacho et al. (2000) estimates a 3D density-contrast distribution using a systematic search to iteratively "grow" the solution, one prismatic element at a time, from a starting distribution with zero density contrast. At each iteration a new prismatic element is added to the estimate with a prespecified positive or negative density contrast. This new prismatic element is chosen by systematically searching the set of all prisms that still have zero density contrast for the one whose incorporation into the estimate minimizes a goal function composed of the data-misfit function plus the ℓ_2 -norm of the weighted 3D density-contrast distribution. Also belonging to the class of systematic search methods is René (1986), which is able to recover 2D compact bodies (i.e., with no hollows inside) with sharp contacts by successively incorporating new prisms around user-specified prisms called seeds. These seeds have a given set of density contrasts, all of which must have the same sign. At the first iteration, the new prism that will be incorporated is chosen by systematically searching the set of neighboring prisms of the seeds for the one that minimizes a "shape-of-anomaly" function. From the second iteration on, the search is performed over the set of available neighboring prisms of the current estimate. Thus, the solution grows through the addition of prisms to its periphery, in a manner mimicking the growth of crystals. René's (1986) method is restricted to interpret density-contrast distributions with a single sign and its estimated solution can be allowed to grow in any combination of user-specified directions.

These inversion methods that do not solve linear systems have been applied to the vertical component of the gravity field yielding good results. To our knowledge, such class of methods has not been previously applied to interpret gravity gradiometry data. Beside, these methods are unable to deal with the presence of interfering signals produced by nontargeted sources that can be interpreted as geologic noise. This is a common scenario encountered in complex geologic settings where the signal of nontargeted sources cannot be completely removed from the data. In the literature, few inversion methods have addressed this issue of interpreting only targeted sources when in the presence of nontargeted sources in a geologic setting (e.g., Silva and Holmann, 1983; Silva and Cutrim, 1989; Silva Dias et al., 2007). The typical approach is to require

the interpreter to perform some sort of data preprocessing to remove the signal produced by the nontargeted geologic sources. This preprocessing generally involves filtering the observed data based on the assumed spectral content of the targeted sources. However, separating the signal of multiple sources often is impractical, if not impossible. An effective way to overcome this problem is to devise an inversion method that simultaneously estimates targeted geologic sources and reduces the undesired effects produced by the nontargeted sources by means of a robust data-fitting procedure. Silva and Holmann (1983) and Silva and Cutrim (1989), for example, minimized, respectively, the ℓ_1 -norm and the Cauchy-norm of the residuals (the difference between the observed and predicted data) to take into account the presence of nontargeted sources. Both data-fitting procedures are more robust than the typical least-squares approach of minimizing the ℓ_2 -norm of the residuals because they allow the presence of large residual values.

We present a new gravity gradient inversion for estimating a 3D density-contrast distribution belonging to the class of methods that do not solve linear systems, but instead implement a systematic search algorithm. Like René (1986), we incorporate prior information into the solution using seeds (i.e., user-specified prismatic elements) around which the solution grows. In contrast with René's (1986) method, our approach can be used to interpret multiple geologic sources with density contrasts of different signs. This is possible because our approach allows assigning a different density contrast to each seed and does not impose any restrictions on the sign of the gravity anomaly. We impose compactness on the solution using a modified version of the regularizing function proposed by Silva Dias et al. (2009). We use as a data-misfit function the ℓ_1 -norm of the residuals because it tolerates large data residuals. This is a desirable feature of the ℓ_1 -norm because it means that it is less influenced by outliers in the observed data and nontargeted sources. Therefore, our approach requires neither substantial amounts of prior information about the nontargeted sources nor the isolation of the effect of the targeted sources through preprocessing. Finally, we exploit the fact that our systematic search is limited to the neighboring prisms of the current estimate to implement a lazy evaluation (Henderson and Morris, 1976) of the sensitivity matrix, thus achieving a fast and memory efficient inversion. Tests on synthetic data and on airborne gravity gradiometry data collected over the Quadrilátero Ferrífero, southeastern Brazil, confirmed the potential of our method in producing sharp images of the targeted anomalous density distribution (iron orebody) in the presence of nontargeted sources.

METHODOLOGY

Let $\mathbf{g}^{\alpha\beta}$ be an L -dimensional vector that contains observed values of the $g_{\alpha\beta}$ -component of the gravity gradient tensor, where α and β belong to the set of x -, y -, and z -directions of a right-sided Cartesian coordinate system (Figure 1). We define this coordinate system with its x -axis pointing north, y -axis pointing east, and z -axis pointing down. We assume that $\mathbf{g}^{\alpha\beta}$ is caused by an anomalous density distribution contained within a 3D region of the subsurface. This region can be discretized into juxtaposed 3D right rectangular prisms composing an interpretative model (Figure 1). Each prism in this model has a homogeneous density contrast and the resulting piecewise-constant anomalous density distribution is assumed to be sufficient to approximate the true one. It follows that the $g_{\alpha\beta}$ -component of the gravity gradient tensor produced by the

anomalous density distribution can be approximated by the sum of the contributions of each prism of the interpretative model, i.e.,

$$\mathbf{d}^{\alpha\beta} = \sum_{j=1}^M p_j \mathbf{a}_j^{\alpha\beta}. \quad (1)$$

This linear relationship can be written in matrix notation as

$$\mathbf{d}^{\alpha\beta} = \mathbf{A}^{\alpha\beta} \mathbf{p}, \quad (2)$$

where \mathbf{p} is an M -dimensional vector whose j th element, p_j , is the density contrast of the j th prism of the interpretative model, $\mathbf{d}^{\alpha\beta}$ is an L -dimensional vector of data predicted by \mathbf{p} , which one would expect approximates $\mathbf{g}^{\alpha\beta}$, and $\mathbf{A}^{\alpha\beta}$ is the $L \times M$ sensitivity matrix, whose j th column is the L -dimensional vector $\mathbf{a}_j^{\alpha\beta}$. The i th element of $\mathbf{a}_j^{\alpha\beta}$ is numerically equal to the $g_{\alpha\beta}$ -component of the gravity gradient tensor caused by the j th prism of the interpretative model, with unit density contrast, calculated at the place where the i th observation was made. It is then evident that the j th column of the sensitivity matrix represents the influence that p_j has on the predicted data. The elements of matrix $\mathbf{A}^{\alpha\beta}$ can be calculated using the formulas of Nagy et al. (2000).

Let $\mathbf{r}^{\alpha\beta}$ be the L -dimensional residual vector of the $g_{\alpha\beta}$ -component of the gravity gradient tensor, i.e.,

$$\mathbf{r}^{\alpha\beta} = \mathbf{g}^{\alpha\beta} - \mathbf{d}^{\alpha\beta}. \quad (3)$$

We define the data-misfit function $\phi_{\alpha\beta}(\mathbf{p})$ of the $g_{\alpha\beta}$ -component of the gravity gradient tensor as a norm of the residual vector $\mathbf{r}^{\alpha\beta}$. For a least-squares fit, $\phi_{\alpha\beta}(\mathbf{p})$ is defined as the ℓ_2 -norm of the residual

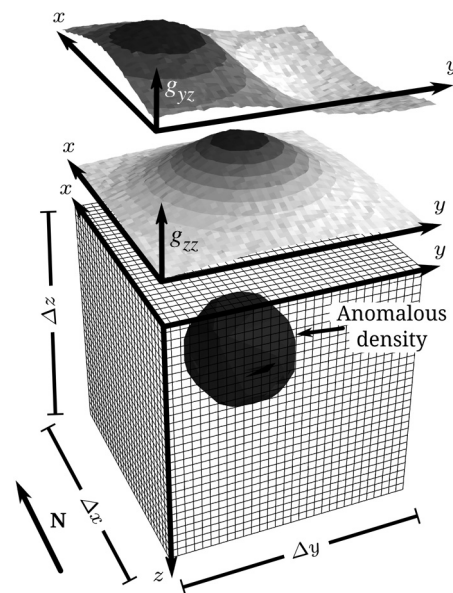


Figure 1. Schematic representation of the interpretative model consisting of a grid of M juxtaposed 3D right-rectangular prisms. The interpretative model used to parametrize the anomalous density distribution is shown in gray. The observed g_{yz} - and g_{zz} -components of the gravity gradient tensor produced by the anomalous density distribution are shown in gray-scale contour maps. Δx , Δy , and Δz are the lengths of the interpretative model in the x -, y -, and z -dimensions, respectively.

vector. The least-squares fit distributes the residuals assuming that the errors in the data follow a short-tailed Gaussian distribution and thus sporadically large residual values are highly improbable (Claerbout and Muir, 1973; Silva and Holmann, 1983; Menke, 1989; Tarantola, 2005). Hence, the ℓ_2 -norm is known to be sensitive to outliers in the data, which can result from either gross errors or geologic noise (i.e., anomalous densities which are not of interest to the interpretation). On the other hand, if occasional large residuals are desired in the inversion, one can use the ℓ_1 -norm of the residual vector. Here, we have chosen the normalized ℓ_1 -norm of the L -dimensional residual vector $\mathbf{r}^{\alpha\beta}$, hence, the data-misfit function is defined as

$$\phi_{\alpha\beta}(\mathbf{p}) = \frac{\|\mathbf{r}^{\alpha\beta}\|_1}{\|\mathbf{g}^{\alpha\beta}\|_1} = \frac{\sum_{i=1}^L |g_i^{\alpha\beta} - d_i^{\alpha\beta}|}{\sum_{i=1}^L |g_i^{\alpha\beta}|}. \quad (4)$$

In this case, the errors in the data are assumed to follow a long-tailed Laplace distribution and a more robust fit is obtained because the predicted data will be insensitive to outliers.

Let us assume that there are N_c -components of the gravity tensor available. Hence, the total data-misfit function $\Phi(\mathbf{p})$ can be defined as the sum of the individual data-misfit functions for each of the N_c -components, i.e.,

$$\Phi(\mathbf{p}) = \sum_{k=1}^{N_c} \phi_k(\mathbf{p}), \quad (5)$$

where $\phi_k(\mathbf{p})$ is the k th function in the set of N_c available data-misfit functions. For example, if the available components are g_{xx} , g_{yy} , and g_{zz} , in that order, then $N_c = 3$ and $\phi_1(\mathbf{p}) \equiv \phi_{xx}(\mathbf{p})$, $\phi_2(\mathbf{p}) \equiv \phi_{yy}(\mathbf{p})$, and $\phi_3(\mathbf{p}) \equiv \phi_{zz}(\mathbf{p})$, all given by equation 4.

Regardless of the norm used in the data-misfit function, the inverse problem of estimating a 3D density-contrast distribution from gravity gradiometry data is ill-posed and requires additional constraints to be transformed into a well-posed problem with a unique and stable solution. The constraints chosen for our method are:

Constraint 1:

The solution should be compact (i.e., without any hollows inside it).

Constraint 2:

The excess (or deficiency of) mass contained in the solution should be concentrated around user-specified prisms of the interpretative model with known density contrasts (referred to as “seeds”).

Constraint 3:

The only density-contrast values allowed are zero or the values assigned to the seeds.

Constraint 4:

Each element of the solution should have the density contrast of the seed closest to it.

We solve the constrained inverse problem of estimating a parameter vector \mathbf{p} subject to these constraints through an iterative algorithm named “planting algorithm,” as explained bellow. At each iteration, this algorithm evaluates the goal function

$$\Gamma(\mathbf{p}) = \Phi(\mathbf{p}) + \mu\theta(\mathbf{p}), \quad (6)$$

where $\theta(\mathbf{p})$ is a regularizing function defined in the parameter (model) space that imposes physical and/or geologic attributes on the solution. The scalar μ is a regularizing parameter that balances the tradeoff between the total data-misfit function $\Phi(\mathbf{p})$ (equation 5) and the regularizing function $\theta(\mathbf{p})$. The regularizing function $\theta(\mathbf{p})$ is an adaptation of the one used in Silva Dias et al. (2009), which in turn is a modified version of the one used by Guillen and Menichetti (1984) and Silva and Barbosa (2006). It enforces the compactness of the solution and the concentration of mass around the seeds (i.e., constraints 1 and 2), being defined as

$$\theta(\mathbf{p}) = \frac{1}{f} \sum_{j=1}^M \frac{p_j}{p_j + \epsilon} l_j, \quad (7)$$

where p_j is the j th element of \mathbf{p} , l_j is the distance between the center of the j th prism and the center of a seed (see subsection Planting algorithm), ϵ is a small positive scalar used to avoid a singularity when $p_j = 0$, and the scalar f is the average extent of the interpretative model, defined as

$$f = \frac{\Delta x + \Delta y + \Delta z}{3}, \quad (8)$$

where Δx , Δy , and Δz are the lengths of the interpretative model in the x -, y -, and z -directions, respectively (Figure 1).

In practice, the scalar ϵ (equation 7) is not necessary because one can add either zero or l_j when evaluating the regularizing function. Furthermore, the value of the regularizing parameter μ should be selected through trial and error. A small value of μ is not able to estimate compact sources, whereas a large value of μ produces compact solutions that might not fit the observed data. To determine an adequate value for μ , we start with a small value, typically 10^{-5} . Then, if needed, the value is raised until the estimated density-contrast distribution achieves the desired compactness.

The two remaining constraints (3 and 4) are imposed algorithmically, as explained bellow.

Planting algorithm

Our systematic search algorithm, named planting algorithm, requires that a set of N_s seeds and their associated density-contrast values be specified by the user. Each seed is a prism of the interpretative model. We emphasize that the density-contrast values of the seeds do not need to be the same. These seeds should be chosen according to prior information about the targeted anomalous sources, such as those provided by the available geologic models, well logs, and interpretations using other geophysical data sets. The planting algorithm starts with an initial parameter vector that includes the density-contrast values assigned to the seeds and has all other elements set to zero (Figure 2a). Hence, by recalling equations 1 and 3, we can define the initial residual vector of the $g_{\alpha\beta}$ -component of the gravity gradient tensor as

$$\mathbf{r}_{(0)}^{\alpha\beta} = \mathbf{g}^{\alpha\beta} - \left(\sum_{s=1}^{N_s} \rho_s \mathbf{a}_{js}^{\alpha\beta} \right), \quad (9)$$

where ρ_s is the density contrast of the s th seed, j_s is the corresponding index of the s th seed in the parameter vector \mathbf{p} , and $\mathbf{a}_{j_s}^{\alpha\beta}$ is the L -dimensional column vector of the sensitivity matrix $\mathbf{A}^{\alpha\beta}$ (equation 2) corresponding to the s th seed. We can then proceed to calculate the initial total data-misfit function $\Phi_{(0)}$ (equation 5), which depends on $\mathbf{r}_{(0)}^{\alpha\beta}$.

The solution to the constrained inverse problem is then built through an iterative growth process. Initially, to each seed is assigned a list of its neighboring prisms (prisms that share a face with the seed). An iteration of the growth process consists of attempting to grow, one at a time, each of the N_s seeds by performing the accretion of a prism from the seed's list of neighboring prisms. We define the accretion of a prism as changing its density-contrast value from zero to the density contrast of the seed undergoing the accretion, guaranteeing constraint 3. Thus, a growth iteration is composed of at most N_s accretions, one for each seed. Furthermore, constraint 4 is guaranteed because only prisms from the list of neighboring prisms of the seed undergoing the accretion are eligible to be accreted to that seed.

The choice of a neighboring prism for the accretion to the s th seed follows two criteria:

- The addition of the neighboring prism to the current estimate should reduce the total data-misfit function $\Phi(\mathbf{p})$ (equation 5), as compared with the previous accretion iteration. This ensures that the solution grows in a way that best fits the observed data. To avoid an exaggerated growth of the estimated anomalous densities, the algorithm does not perform the accretion of neighboring prisms that produce very small changes in the total data-misfit function. The criterion for how small a change is accepted is based on whether the following inequality holds:

$$\frac{|\Phi_{(\text{new})} - \Phi_{(\text{old})}|}{\Phi_{(\text{old})}} \geq \delta, \quad (10)$$

where $\Phi_{(\text{new})}$ is the total data-misfit function evaluated with the chosen neighboring prism included in the estimate, $\Phi_{(\text{old})}$ is the total data-misfit function evaluated during the previous accretion iteration, and δ is a positive scalar typically ranging from 10^{-3} to 10^{-6} . Parameter δ controls how much the anomalous densities are allowed to grow. The choice of the value of δ depends on the size of the prisms of the interpretative model. The smaller the prisms are, the smaller their contribution to $\Phi(\mathbf{p})$ will be, and thus, the smaller δ should be.

- The addition of the neighboring prism with density contrast ρ_s to the current estimate should produce the smallest value of the goal function $\Gamma(\mathbf{p})$ (equation 6) out of all other prisms in the list of neighboring prisms of the s th seed that obeyed the first criterion. Thus, the accretion of the neighboring prism to the current estimate will produce the highest decrease in the

total data-misfit function (equation 5) as well as the lowest increase in the regularizing function $\theta(\mathbf{p})$ (equation 7). This ensures that constraints 1, 2, and 4 are met. We clarify here that the term l_j in equation 7 is the distance between the center of the j th prism and the center of the s th seed (i.e., the one that is undergoing the accretion). We stress that the j th prism belongs to the list of neighboring prisms of the s th seed.

Once the accretion of the j th prism is performed to the s th seed, the neighboring prisms of the j th prism are included in the s th seed's list of neighboring prisms and the j th prism is removed from this list (Figure 2b). It is important to note that the list of seeds is not modified along the iterations of our algorithm. Rather, the list of neighboring prisms of a seed varies each time it suffers an accretion. Finally, we update the residual vectors of the N_c available components. The updated residual vector of the $g_{\alpha\beta}$ -component of the gravity gradient tensor is given by

$$\mathbf{r}_{(\text{new})}^{\alpha\beta} = \mathbf{r}_{(\text{old})}^{\alpha\beta} - p_j \mathbf{a}_j^{\alpha\beta}, \quad (11)$$

where $\mathbf{r}_{(\text{new})}^{\alpha\beta}$ is the updated residual vector, $\mathbf{r}_{(\text{old})}^{\alpha\beta}$ is the residual vector evaluated in the previous accretion iteration, j is the index of the neighboring prism chosen for the accretion, $p_j = \rho_s$, and $\mathbf{a}_j^{\alpha\beta}$ is the j th column vector of the sensitivity matrix $\mathbf{A}^{\alpha\beta}$. In the case that none of the neighboring prisms of the s th seed meet the first criterion, the s th seed does not grow during this growth iteration. This ensures that different seeds can produce anomalous densities of different sizes. The growth process continues while at least one of the seeds is able to grow. At the end of the growth process, our planting algorithm should yield a solution composed of compact anomalous densities with variable sizes (Figure 2c). Uieda and Barbosa (2012a) show an animation of this growth process when the planting algorithm is applied to synthetic data of the g_{zz} -component of the gravity gradient tensor.

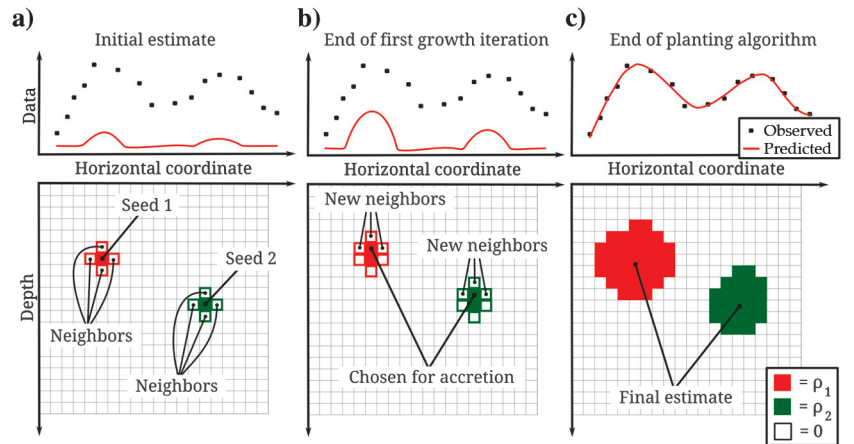


Figure 2. Two-dimensional sketch of three stages of the planting algorithm. Black dots represent the observed data and the red line represents the predicted data produced by the current estimate. The light gray grid of prisms represents the interpretative model. (a) Initial state with the user-specified seeds included in the estimate with their corresponding density contrasts and all other parameters set to zero. (b) End of the first growth iteration where two accretions took place, one for each seed. The list of neighboring prisms of each seed and the predicted data are updated. (c) Final estimate at the end of the algorithm. The growth process stops when the predicted data fits the observed data.

Lazy evaluation of the sensitivity matrix

In our planting algorithm, all elements of the parameter vector not corresponding to the seeds start with zero density contrast. It is then noticeable from equations 1 and 9 that the columns of the sensitivity matrices $\mathbf{A}^{a\beta}$ that do not correspond to the seeds are not required for the initial computations. Moreover, the search for the next element of the parameter vector for the accretion is restricted to the list of neighboring prisms of the seeds. This means that the j th column vectors $\mathbf{a}_j^{a\beta}$ of the sensitivity matrices only need to be calculated once the j th prism of the interpretative model becomes eligible for accretion (i.e., becomes a member of the list of neighboring prisms of a seed). In addition, our algorithm updates the residual vectors after each successful accretion through equation 11. Once the j th prism is permanently incorporated into the current solution, the column vectors $\mathbf{a}_j^{a\beta}$ are no longer needed. Thus, the full sensitivity matrices $\mathbf{A}^{a\beta}$ are not needed at any single time during the growth process. Column vectors of $\mathbf{A}^{a\beta}$ can be calculated on demand and deleted once they are no longer required (i.e., after an accretion). This technique is known in computer science as a “lazy evaluation” (Henderson and Morris, 1976). Because the computation of the full sensitivity matrix is a time- and memory-consuming process, the implementation of a lazy evaluation of $\mathbf{A}^{a\beta}$ leads to fast inversion times and low memory usage, making viable the inversion of large data sets using fine grids of prisms for the interpretative models without needing supercomputers or data compression algorithms (e.g., Portniaguine and Zhdanov, 2002).

Presence of nontargeted sources

In real world scenarios, there are interfering signals produced by multiple and horizontally separated sources (Figure 3a). Some of

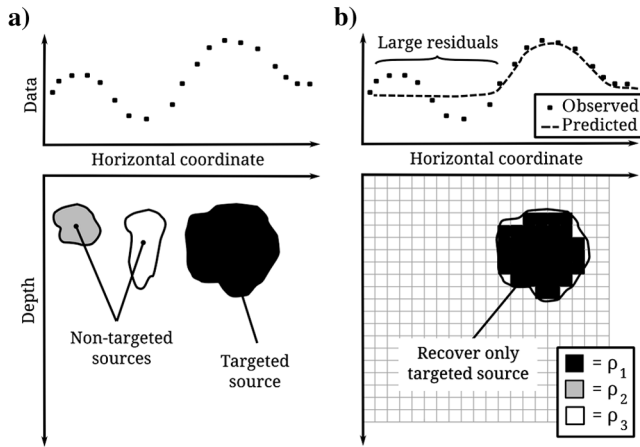


Figure 3. Two-dimensional sketch of the robust procedure. Black dots represent the observed data produced by (a) the true sources with different density contrasts ρ_1 , ρ_2 , and ρ_3 (black, gray, and white polygons, respectively). The gray and white sources are considered nontargeted sources. The white source has a density contrast with the opposite sign of the black and gray sources. (b) Inversion result when given a seed only for the targeted source (black polygon) and using the ℓ_1 -norm of the residual vector (equation 4). The dashed line in (b) represents the data predicted by the inversion result. Large residuals over the nontargeted sources are automatically allowed by the inversion. The estimated density-contrast distribution (black prisms) recovers only the shape of the targeted source (black outline).

these sources may be of no interest to the interpretation (i.e., nontargeted sources) or there may not be enough available prior information about them, like their approximate depths or density contrasts. Furthermore, in most cases, it is not possible to separate the signal of the targeted and the nontargeted sources. It would then be desirable to provide seeds only for the targeted sources and that the estimated density-contrast distribution could be obtained without being affected by the signal of the nontargeted sources. For this purpose, one can use the ℓ_1 -norm of the residual vector (equation 4) to allow large residual values in the signal that is most influenced by the nontargeted sources (Figure 3b). Thus, the inversion is less influenced by the signal yielded by the nontargeted sources by treating it as outliers in the data. Note that the ℓ_1 -norm by itself does not “know” which parts of the data should be treated as outliers. This information is indirectly incorporated into the inversion through the locations of the seeds provided for the targeted sources only. Therefore, the ℓ_1 -norm has to be used in conjunction with the strong mass-concentration constraints imposed by the regularizing function (equation 7).

This robust procedure allows one to choose the targets of the interpretation without having to isolate their signal before performing the inversion. It also eliminates the need for prior information about the density contrast and approximate depth of the nontargeted sources, although their approximate horizontal locations are still required. Additionally, by using the ℓ_1 -norm of the residual vector, we can also handle noisy outliers in the data, such as instrumental or operational errors.

APPLICATION TO SYNTHETIC DATA

We applied our method to synthetic noise-corrupted data of the g_{yy} -, g_{yz} -, and g_{zz} -components of the gravity gradient tensor. Figure 4a shows a color-scaled map of the synthetic g_{zz} -component. Color-scaled maps of the g_{yy} - and g_{yz} -components are provided in Figure 1 of the supplementary material of Uieda and Barbosa (2012b). The synthetic data were produced by 11 rectangular parallelepipeds (Figure 5a) with density contrasts ranging from -1 to 1.2 g/cm³. Each component was calculated on a regular grid of 51×51 observation points in the x - and y -directions, totaling

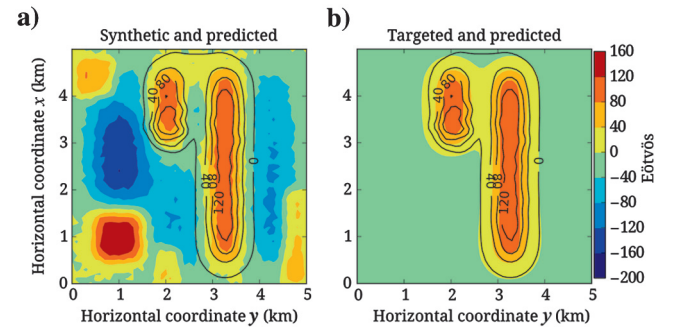


Figure 4. Test with synthetic data produced by multiple targeted and nontargeted sources. (a) Synthetic noise-corrupted data (color-scale map) and data predicted by the inversion result (black contour lines) of the g_{zz} -component of the gravity gradient tensor. The synthetic data were produced by the 11 sources shown in Figure 5a. The predicted data is produced by the inversion result shown in Figure 5c. (b) The g_{zz} -component of the gravity gradient tensor produced only by the targeted sources (color-scale map) and the same data predicted by the inversion result in Figure 5c (black contour lines).

7,803 observations, with a grid spacing of 0.1 km along both directions. We corrupted the synthetic data with pseudorandom Gaussian noise with zero mean and 5 Eötvös standard deviation.

To demonstrate the efficiency of our method in retrieving only the targeted sources even in the presence of nontargeted ones, we chose only the sources with density contrast of 1.2 g/cm^3 (red blocks in Figure 5a) as targets of the interpretation. Thus, we specified the set of 13 seeds shown in Figure 5b (nine for the largest source and four for the smallest one) and used the ℓ_1 -norm of the residual vector (equation 4) to ignore the signal of the nontargeted sources (all sources with density contrast different from 1.2 g/cm^3) displayed as blue and yellow blocks in Figure 5a. The inversion was performed using an interpretative model consisting of 37,500 juxtaposed rectangular prisms, $\mu = 10^{-1}$, and $\delta = 10^{-4}$. We used the g_{yy} - and g_{yz} -components, as well as g_{zz} because these two components emphasize the signal of the targeted sources, which are elongated in the x -direction.

Figure 4a shows the predicted data (black contour lines) of the g_{zz} -component produced by the estimated density-contrast distribution shown in Figure 5c. The predicted data of the g_{yy} - and g_{yz} -components are provided in Figure 1 of the supplementary material of Uieda and Barbosa (2012b). By comparing the density-contrast estimates (Figure 5c) with the true targeted sources (red blocks in Figure 5a), we verify the good performance of our method in recovering targeted sources in the presence of nontargeted sources (blue and yellow blocks in Figure 5a) yielding interfering signals. The most striking feature of this inversion result is that it required neither prior information about the density contrasts and approximate depths of the nontargeted sources nor a signal separation to isolate the effect of the targeted sources. For comparison, Figure 4b shows a colored-contour map of the g_{zz} -component of the gravity gradient tensor produced by the targeted sources only (red blocks in Figure 5a) plotted against the predicted data (black contour lines in Figure 4a, and 4b) produced by the estimated density-contrast distribution (Figure 5c). Notice that the inversion performed on the synthetic data set produced by targeted and nontargeted sources (color-scale map in Figure 4a) was able to fit the isolated signals produced by the targeted sources as shown in Figure 4b (black contour lines). These results confirm the ability of our method to tolerate the large residuals caused by the nontargeted sources and successfully recover the targets of the interpretation. Furthermore, when performed on a standard laptop computer with an Intel® Core™ 2 Duo P7350 2.0 GHz processor, the total time for the inversion was approximately 46 seconds.

In Uieda and Barbosa (2012b), we also present a synthetic example illustrating the use of the normalized ℓ_2 -norm of the residual vector (equation 3) in the data-mist function in a geologic setting composed of targeted sources only.

SENSITIVITY ANALYSIS

We present two analyses of important characteristics of our method. In the first one, we investigate the sensitivity of our method to uncertainties in the a priori information (i.e., location and density contrasts of the seeds). In the second analysis, we investigate the limitations of the robust procedure that was proposed to deal with the presence of nontargeted sources. For these purposes, we have conducted various tests on synthetic noise-corrupted data produced by two contiguous sources: a larger dipping source with density contrast of 1 g/cm^3 , and a smaller cubic source with density

contrast of -1 g/cm^3 (black outline in Figures 6, 7, 8, and 9). The depth to the tops of both sources is 0.2 km. All tests were undertaken on the g_{xx} -, g_{xy} -, g_{xz} -, g_{yy} -, g_{yz} -, and g_{zz} -components of the gravity gradient tensor, which were computed at 150 m height on a

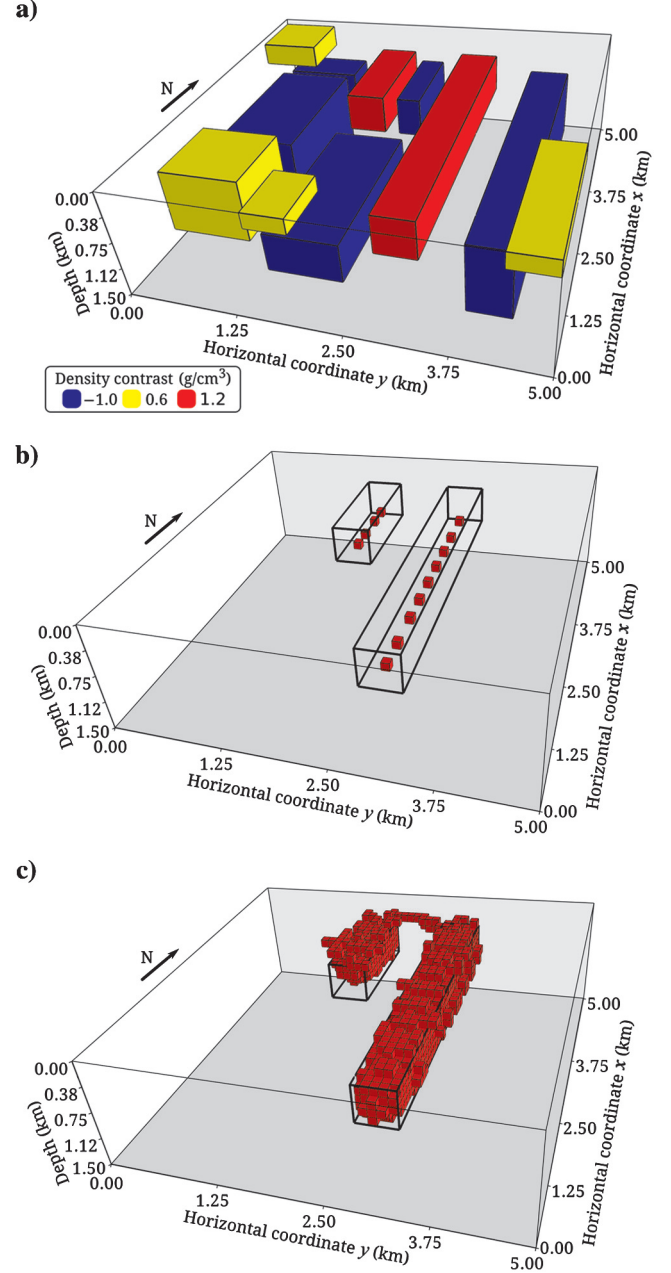


Figure 5. Test with synthetic data produced by multiple targeted and nontargeted sources. (a) Perspective view of the synthetic model used to generate the synthetic data. Only sources with density contrast 0.6 g/cm^3 (yellow) are outcropping. The sources with density contrast 1.2 g/cm^3 (red) were considered as the targets of the interpretation. (b) Seeds used in the inversion and outline of the true targeted sources. (c) Inversion result obtained by using the ℓ_1 -norm of the residual vector (equation 4). Prisms of the interpretative model with zero density contrast are not shown. Black lines represent the outline of the true targeted sources.

regular grid of 31×31 observation points and with grid spacing of 1 km along the x - and y -directions. The data were contaminated with pseudorandom Gaussian noise with zero mean and standard deviation of 0.5 Eötvös. The interpretative model used in the inversions consists of 27,000 juxtaposed right rectangular prisms. In all tests, only the large dipping source was the target of the interpretation. In the first test, we assigned three seeds (gray prisms in the inset of Figure 6) with density contrast of 1 g/cm^3 to the targeted dipping source. These seeds have ideal locations and correctly describe the true framework of the targeted source. Figure 6 shows the

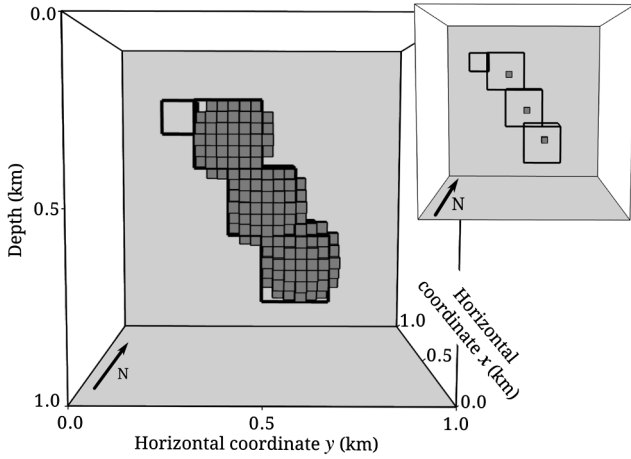


Figure 6. Sensitivity analysis. Test using ideal seed locations and the correct density contrast of 1 g/cm^3 . The outline of the true sources is shown in solid black lines. The inversion result is shown as gray prisms. Prisms with zero density contrast are not shown. The inset shows the three seeds used in the inversion (gray prisms). The location of the seeds was chosen to outline the correct dip of the large dipping source (targeted source).

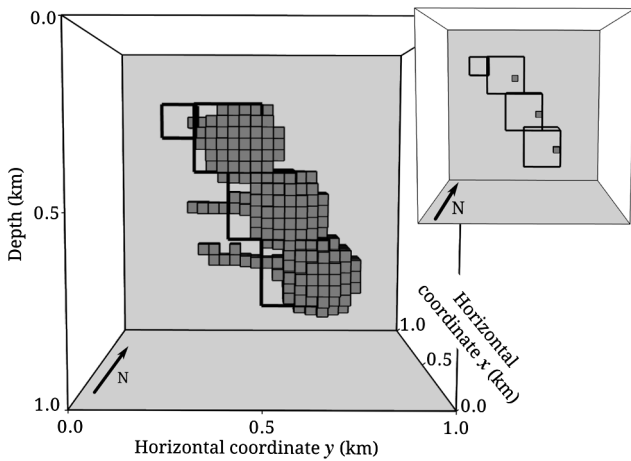


Figure 7. Analysis of the sensitivity to uncertainties in the location of the seeds. Test using three seeds with the correct density contrast of 1 g/cm^3 but with incorrect dip. The outline of the true sources is shown in solid black lines. The inversion result is shown as gray prisms. Prisms with zero density contrast are not shown. The inset shows the three seeds used in the inversion (gray prisms), which had the incorrect dip of the large dipping source (targeted source).

estimated density-contrast distribution obtained by setting the inversion control variables $\mu = 1$ and $\delta = 10^{-4}$. This result demonstrates the excellent performance of our method in recovering the true target dipping source in the presence of the nontargeted cubic source with density contrast of -1 g/cm^3 . The standard deviation of the residual vector of the g_{zz} -component (equation 3) is 0.54 Eötvös, which shows that the predicted data fit the synthetic data within the data error level of 0.5 Eötvös that was used to contaminate the data. This test represents an ideal scenario and will be used as a baseline for comparison with subsequent tests.

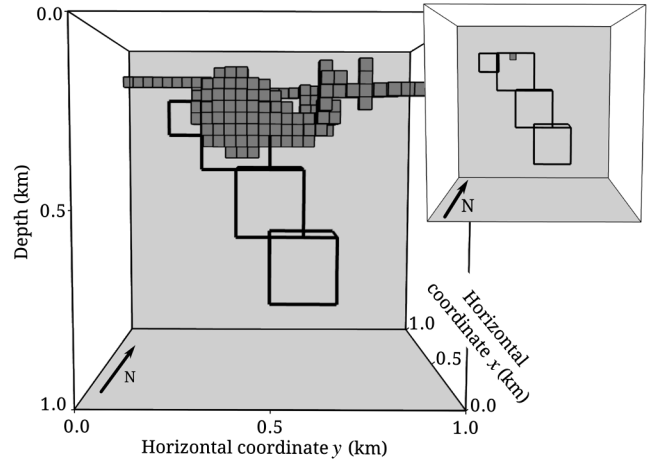


Figure 8. Analysis of the sensitivity to the reduction of the number of seeds. Test using only a single seed and the correct density contrast of 1 g/cm^3 . The outline of the true sources is shown in solid black lines. The inversion result is shown as gray prisms. Prisms with zero density contrast are not shown. The inset shows the single seed used in the inversion (gray prism), which was located at the top of the large dipping source (targeted source).

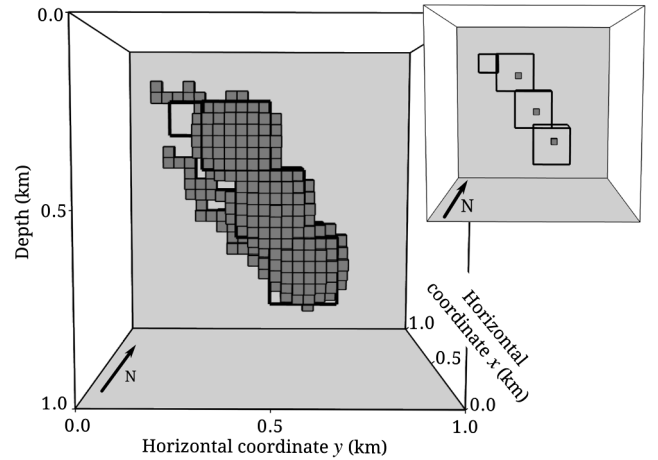


Figure 9. Analysis of the limitations of the robust procedure. In this test, the smaller cubic source (nontargeted source) has a density contrast of 1.5 g/cm^3 , which has the same sign as the density contrast of the larger dipping source (targeted source). Test using three seeds in ideal locations (same as used in Figure 6) with the correct density contrast of 1 g/cm^3 . The inversion result is shown as gray prisms. Prisms with zero density contrast are not shown. The outline of the true sources is shown in solid black lines. The inset shows the three seeds used in the inversion (gray prisms).

The second test was designed to assess the sensitivity of the planting algorithm to uncertainties in the density-contrast value of the targeted sources. Thus, we used the same seed locations and inversion control variables as in the first test, but assigned density contrasts to the seeds that were smaller and larger than the true value. The standard deviation of the residual vector of the g_{zz} -component was 0.53 Eötvös, for the case with a smaller density contrast, and 0.56 Eötvös, for the case with a larger density contrast. Hence, in both cases, the predicted data fit the synthetic data within the assumed data error level. Furthermore, the estimated density-contrast distributions (see Figures 2 and 3 in the supplementary material of Uieda and Barbosa, 2012b) are compact and present the correct dip of the targeted dipping source. However, by assigning a density contrast smaller than the true one, the estimated density-contrast distribution (see Figure 2 in Uieda and Barbosa, 2012b) displays a larger volume when compared with the true source. On the other hand, by assigning a density contrast larger than the true one, the estimated density-contrast distribution (see Figure 3 in Uieda and Barbosa, 2012b) has a smaller volume when compared with the true source.

The third test had the purpose of assessing the sensitivity of our method to the wrong positioning of the seeds that define framework of the targeted source. For this purpose, we used three seeds (gray prisms in the inset of Figure 7) with the correct density contrast of 1 g/cm³ but with their positions defining the wrong dip of the true targeted dipping source. We set $\mu = 1$ and $\delta = 10^{-4}$. Despite the error in defining the locations of the seeds, the estimated density-contrast distribution (Figure 7) still retains the main feature of the true targeted source. However, the solution is not compact and the standard deviation of the residual vector of the g_{zz} -component is 0.70 Eötvös, which shows that the predicted data does not explain the synthetic data within the assumed data error level.

In the fourth test, we assessed the sensitivity of our method to a substantial reduction in the number of seeds. Hence, we assigned a single seed (gray prism in the inset of Figure 8) with density contrast of 1 g/cm³. The choice of positioning the seed at the top of the targeted dipping source is based on a hypothetical previous interpretation provided, for example, by Euler deconvolution. We performed several inversions by setting $\delta = 10^{-4}$ and varying μ from 1 to 10^{10} . The estimated density-contrast distribution (Figure 8) is not compact and is not able to reconstruct the true targeted dipping source, even when μ is assigned a large value (e.g., 10^{10}). Additionally, the standard deviation of the residual vector of the g_{zz} -component is 2.01 Eötvös, which shows that the synthetic data are not fitted by the predicted data within the assumed errors.

The fifth test was meant to analyze the limitations of the proposed robust procedure to effectively ignore the interfering signal of the nontargeted cubic source. We kept the targeted dipping source as it was and changed the density-contrast value of the nontargeted cubic source to 1.5 g/cm³. This was done to simulate targeted and nontargeted sources with density contrasts of the same sign. We used the same seeds as in the first test (inset of Figure 6) with the correct density contrast of 1 g/cm³. These seeds correctly describe the true framework of the targeted dipping source. The inversion was performed using $\mu = 1$ and $\delta = 10^{-4}$. We found that the estimated density-contrast distribution (Figure 9) is not compact and does not retrieve the true targeted source. However, the standard deviation of the residual vector of the g_{zz} -component is 0.71 Eötvös, which

shows that this solution does not explain the synthetic data within the assumed data error level.

Figure 4 of the supplementary material of Uieda and Barbosa (2012b) shows the synthetic noise-corrupted and predicted data of the g_{zz} -component of the gravity gradient tensor for all tests.

APPLICATION TO REAL DATA

One of the most important iron provinces in Brazil is the Quadrilátero Ferrífero (QF), located in the São Francisco Craton, south-eastern Brazil. Most of the iron ore bodies in the QF are hosted in the oxidized, metamorphosed and heterogeneously deformed banded iron formation (BIF) of the Cauê Formation, the so-called itabirites. The itabirites are associated with the Minas Supergroup and contain iron ore oxide facies, such as hematites, magnetites, and martites. We applied our method to estimate the geometry and extent of the iron ore deposits of the Cauê Formation using the data from an airborne gravity gradiometry survey performed in this area (color-scale maps in Figure 10a–10c). The signals associated with the iron ore bodies (targeted sources) are more prominent in the g_{yy} -, g_{yz} -, and g_{zz} -components of the measured gravity gradient tensor (elongated southwest–northeast feature in Figure 10a–10c). This data set also shows interfering signals caused by other sources, which will be considered as nontargeted sources in our interpretation.

The inversion was performed on 4,582 measurements of each of the g_{yy} -, g_{yz} -, and g_{zz} -components of the gravity gradient tensor resulting in a total of 13,746 measurements. We applied our robust procedure to recover only the targeted sources (iron ore bodies) in the presence of the nontargeted sources. Thus, we used the ℓ_1 -norm of the residual vector (equation 4) and provided a set of 46 seeds (black stars in Figure 10) for the targeted iron ore bodies of the Cauê Formation. The horizontal locations of the seeds were chosen based on the peaks of the elongated southwest–northeast positive feature (associated with the iron ore bodies) in the color-scale map of the g_{zz} -component (Figure 10c). The depths of the seeds were chosen based on borehole information and previous geologic interpretations of the area. We assigned a density-contrast value of 1 g/cm³ for the seeds because the data were terrain corrected using a density of 2.67 g/cm³ and the assumed density of the iron ore deposits is 3.67 g/cm³. The interpretative model was formed by a regular mesh cropped to the area of interest and consists of 164,892 prisms which follow the topography of the area (Figure 11a). The inversion was performed using $\mu = 0.1$ and $\delta = 5 \times 10^{-5}$.

The estimated density-contrast distribution corresponding to the iron ore bodies of the Cauê itabirite is shown in red in Figure 11. Cross sections of the estimated density contrast distribution (Figure 12) show that the estimated iron ore bodies are compact and have nonoutcropping parts. Figure 10d–10f shows the predicted data caused by the estimated density-contrast distribution shown in Figure 11. For all three components, the inversion is able to fit the elongated southwest–northeast feature associated with the iron ore deposits (targeted sources) and successfully ignore the other signals presumably produced by the nontargeted sources (Figure 10). These results show the ability of our method to provide a compact estimate of the iron ore deposits. We emphasize that this was possible without prior information about the density contrasts and approximate depths of the nontargeted sources and without isolating the signals produced by the targeted sources. All

these requirements would be impractical in this highly complex geologic setting. Our results are in close agreement with previous interpretations by [Martinez et al. \(2010\)](#). Furthermore, when performed on a standard laptop computer, the total time for the inversion was approximately 14 minutes.

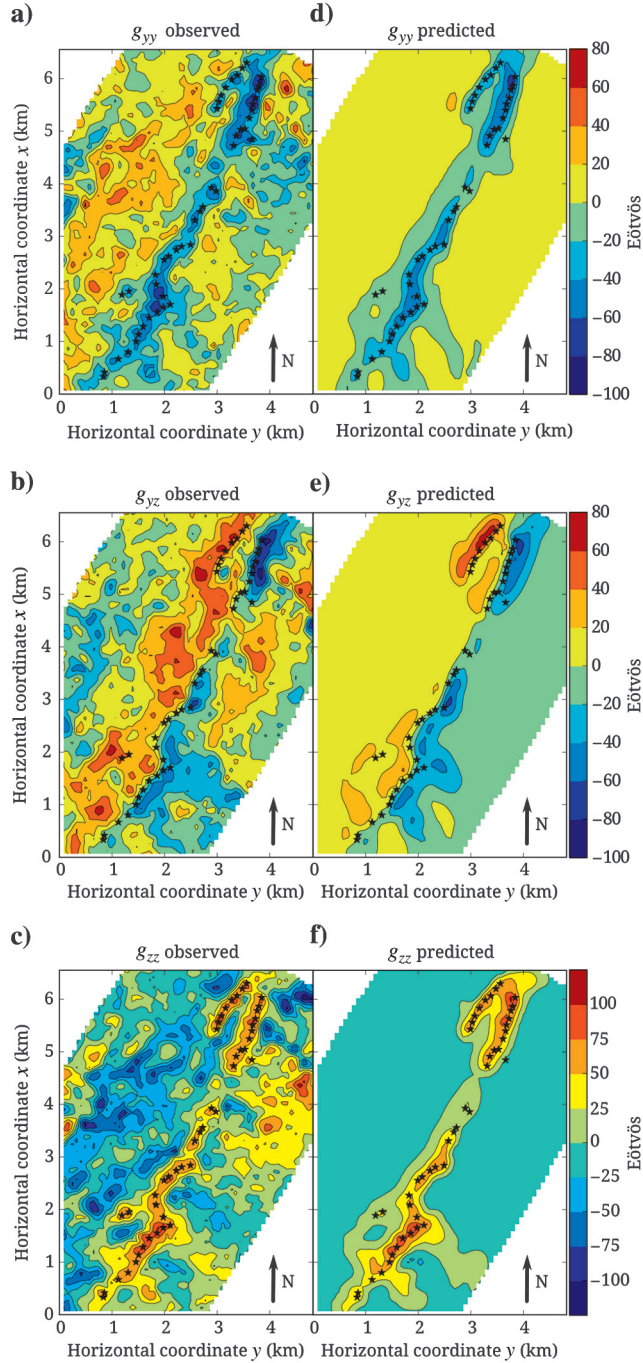


Figure 10. Application to real data from an airborne gravity gradiometry survey over a region of the Quadrilátero Ferrífero, southeastern Brazil. The observed (a-c) and predicted (d-f) g_{yy} -, g_{yz} -, and g_{zz} -components of the gravity gradient tensor. The latter were produced by the estimated density-contrast distribution shown in Figure 11. Black stars represent the horizontal coordinates of the seeds used in the inversion.

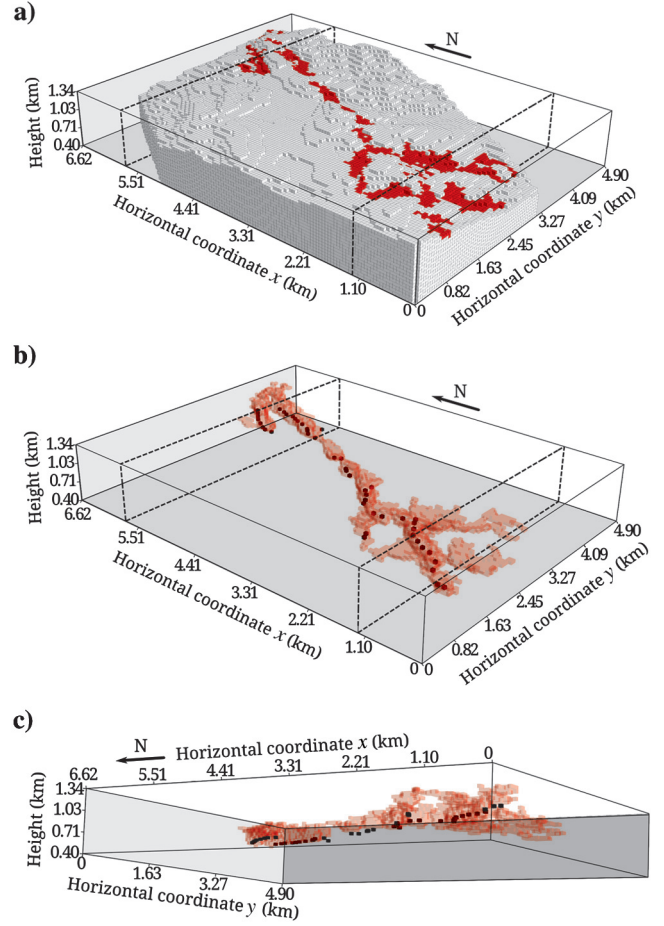


Figure 11. Results from the application to real data from the Quadrilátero Ferrífero, southeastern Brazil. Dashed lines show the location of the cross sections in Figure 12. (a-c) Perspective views of the estimated density-contrast distribution, where prisms with zero density contrast are not shown or shown in gray and prisms with density contrast 1 g/cm^3 , corresponding to the iron orebody of the Cauê itabirite, are shown in solid or transparent red. The seeds used in the inversion are shown as black prisms.

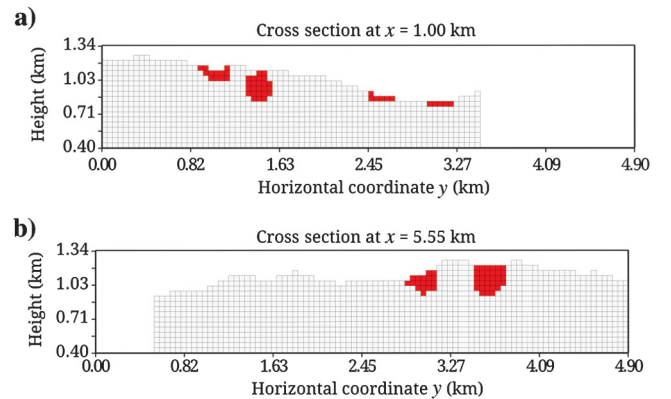


Figure 12. Results from the application to real data from the Quadrilátero Ferrífero, southeastern Brazil. Cross sections of the inversion result shown in Figure 11 at horizontal coordinate x equal to (a) 1.00 km and (b) 5.55 km . Prisms with zero density contrast are shown in gray and prisms with density contrast 1 g/cm^3 , corresponding to the iron orebody of the Cauê itabirite, are shown in red.

DISCUSSION

The proposed inversion method incorporates a priori information into the solution through user-specified seeds. The positions of the seeds determine roughly where the “skeletons” of the estimated targeted sources will be. Whereas, the density-contrast values assigned to the seeds determine the density contrasts of the estimated targeted sources. Therefore, one must provide adequate seeds to obtain good results. In cases where the density-contrast values of the seeds are poorly assigned, the volumes of the estimated sources will be either greater or smaller than the true ones. However, their overall shape and mass do not appear to be affected. Tests on synthetic data (Figures 7 and 8) indicate that a reasonable fit of the observed data is not obtained if the number of seeds used or their positions are inadequate. Moreover, in these cases, our method is not able to estimate compact sources. Rather, the estimated sources exhibit shapes that do not resemble geologic structures, such as the tentacle-like structures shown in Figures 7 and 8. Thus, the presence of these “tentacles” in a solution, combined with a poor fit of the observed data may be used as heuristic criteria to evaluate the correctness of the locations of the seeds. In cases where the errors in the locations are small, the direction in which the tentacles grow may indicate the direction in which lies a better position for the seeds (Figure 7). Thus, the positions of the seeds can be manually adjusted by the user until an acceptable data fit is obtained and the estimated sources are not only compact, but resemble geologic structures. We emphasize that this procedure is only practical because our method is computationally efficient, which is due to the restricted systematic search of the planting algorithm and the lazy evaluation of the sensitivity matrix. An alternative approach to determine the locations of the seeds is to use interpretation methods that estimate the centers of mass of the sources (e.g., Medeiros and Silva, 1995; Beiki and Pedersen, 2010). Medeiros and Silva (1995) achieve this by inverting the source moments obtained from the gravity anomaly. On the other hand, Beiki and Pedersen (2010) use the eigenvectors of the gravity gradient tensor to estimate the coordinates of the centers of mass of the sources. However, we stress that if the fit of the observed data is acceptable and the estimated sources present geologically reasonable shapes, the hypothesis about the seeds must be accepted. Hence, the estimated solution must be accepted as a possible solution, even if it differs from the true one.

Another type of a priori information required by our method is whether or not a given signal is due to the targeted sources. This information is conveyed through the horizontal locations of the seeds associated with the targeted sources only. Because of this information and the mass concentration constraint imposed by the regularizing function (equation 7), the estimated sources cannot grow too far from the seeds. Furthermore, the use of the ℓ_1 -norm of the residual vectors (equation 4) reduces the influence of the signal of the nontargeted sources. Nonetheless, the use of the ℓ_1 -norm alone cannot guarantee the robustness of our method to the presence of nontargeted sources. Tests on synthetic data (Figures 5 and 9) show that the robustness requires some form of “barrier” between the targeted and nontargeted sources. We concluded from our tests that these barriers must be sources with a density contrast of opposite sign of the targeted sources. These barriers work as a natural obstacle for the growth of the estimated density-contrast distribution (Figure 5). We also stress that even in the case where the targeted and nontargeted sources

have opposite signs, the robustness of our method may fail if the signals produced by these sources present a substantial overlap. In this case the estimated volume of the targeted source will be underestimated.

CONCLUSIONS

We have presented a new method for the 3D inversion of gravity gradient data that uses a systematic search algorithm. We parametrized the earth’s subsurface as a grid of juxtaposed right rectangular prisms with homogeneous density contrasts. The estimated density-contrast distribution is then iteratively built through the successive accretion of new elements around user-specified prisms called “seeds.” The choice of seeds is used to incorporate into the solution prior information about the density-contrast values and the approximate location of the sources. Our method is able to retrieve multiple sources with different locations, geometries, and density contrasts by allowing each seed to have a different density contrast. Furthermore, we devised a robust procedure that, in some situations, recovers only targeted sources when in the presence of nontargeted sources that yield interfering signals. Thus, prior information about density contrasts and approximate depths of the nontargeted sources is not required. In addition, the signal of the targeted sources does not need to be previously isolated to perform the inversion. In real world scenarios, both of the previously stated requirements would be highly impractical, or even impossible.

The developed inversion method has low processing time and computer memory usage because there are no matrix multiplications or linear systems to be solved. Further computational efficiency is achieved by implementing a lazy evaluation of the sensitivity matrix. These optimizations make feasible the inversion of the large data sets encountered in airborne gravity gradiometry surveys while using an interpretative model composed of a large number of prisms. Tests on synthetic data and real data from an airborne gravity gradiometry survey show that our method is able to recover compact bodies despite the presence of interfering signals produced by nontargeted sources. However, the developed method requires a substantial amount of prior information. Thus, it is not suitable for interpretations on a regional scale lacking detailed geologic information. Instead, our method should be applied on localized high-resolution interpretations of well constrained targets. This makes our inversion method more suitable to be employed in later stages of an exploration program, when geologic mappings and boreholes are available. Therefore, ideal geologic targets would be compact 3D bodies with sharp boundaries, like salt domes, orebodies, and igneous intrusions.

ACKNOWLEDGMENTS

The authors thank assistant editor Jose Carcione, associate editor Xiong Li, reviewer Gary Barnes, and three anonymous reviewers for their questions and suggestions that greatly improved the original manuscript. We thank Vanderlei C. Oliveira Jr., Dionisio U. Carlos, Irineu Figueiredo, Eder C. Molina, and João B. C. Silva for discussions and insightful comments. We acknowledge the use of plotting library matplotlib by Hunter (2007) and software Mayavi by Ramachandran and Varoquaux (2011). The authors were supported in this research by a fellowship (VCFB) from Conselho Nacional de Desenvolvimento Científico e Tecnológico (CNPq) and a scholarship (LU) from Coordenação de Aperfeiçoamento de Pessoal de Nível Superior (CAPES), Brazil. Additional support for the

authors was provided by the Brazilian agencies CNPq (grant 471693/2011-1) and FAPERJ (grant E-26/103.175/2011). The authors would like to thank Vale for permission to use the gravity gradiometry data of the Quadrilátero Ferrífero.

REFERENCES

- Beiki, M., and L. B. Pedersen, 2010, Eigenvector analysis of gravity gradient tensor to locate geologic bodies: *Geophysics*, **75**, no. 6, 137–149, doi: [10.1190/1.3484098](https://doi.org/10.1190/1.3484098).
- Camacho, A. G., F. G. Montesinos, and R. Vieira, 2000, Gravity inversion by means of growing bodies: *Geophysics*, **65**, 95–101, doi: [10.1190/1.1444729](https://doi.org/10.1190/1.1444729).
- Claerbout, J. F., and F. Muir, 1973, Robust modeling with erratic data: *Geophysics*, **38**, 826–844, doi: [10.1190/1.1440378](https://doi.org/10.1190/1.1440378).
- Cordell, L., 1994, Potential-field sounding using Euler's homogeneity equations and Zidarov bubbling: *Geophysics*, **59**, 902–908, doi: [10.1190/1.1443649](https://doi.org/10.1190/1.1443649).
- Cox, L. H., G. Wilson, and M. S. Zhdanov, 2010, 3D inversion of airborne electromagnetic data using a moving footprint: *Exploration Geophysics*, **41**, 250–259, doi: [10.1071/EG10003](https://doi.org/10.1071/EG10003).
- Guillen, A., and V. Menichetti, 1984, Gravity and magnetic inversion with minimization of a specific functional: *Geophysics*, **49**, 1354–1360, doi: [10.1190/1.1441761](https://doi.org/10.1190/1.1441761).
- Henderson, P., and J. H. Morris Jr., 1976, A lazy evaluator: Proceedings of the 3rd ACM SIGACT-SIGPLAN symposium on Principles on programming languages, ACM, 95–103, doi: [10.1145/800168.811543](https://doi.org/10.1145/800168.811543).
- Hunter, J. D., 2007, Matplotlib: A 2D graphics environment: *Computing in Science & Engineering*, **9**, 90–95, doi: [10.1109/MCSE.2007.55](https://doi.org/10.1109/MCSE.2007.55).
- Jorgensen, G. J., and J. L. Kisabeth, 2000, Joint 3D inversion of gravity, magnetic and tensor gravity fields for imaging salt formations in the deepwater Gulf of Mexico: 70th Annual International Meeting, SEG, Expanded Abstracts, 424–426.
- Krahenbuhl, R. A., and Y. Li, 2009, Hybrid optimization for lithologic inversion and time-lapse monitoring using a binary formulation: *Geophysics*, **74**, no. 6, 155–165, doi: [10.1190/1.3242271](https://doi.org/10.1190/1.3242271).
- Li, Y., 2001, 3D inversion of gravity gradiometer data: 71st Annual International Meeting, SEG, Expanded Abstracts, 1470–1473.
- Li, Y., and D. W. Oldenburg, 1998, 3D inversion of gravity data: *Geophysics*, **63**, 109–119, doi: [10.1190/1.1444302](https://doi.org/10.1190/1.1444302).
- Li, Y., and D. W. Oldenburg, 2003, Fast inversion of large-scale magnetic data using wavelet transforms and a logarithmic barrier method: *Geophysical Journal International*, **152**, 251–265, doi: [10.1046/j.1365-246X.2003.01766.x](https://doi.org/10.1046/j.1365-246X.2003.01766.x).
- Martinez, C., Y. Li, R. Krahenbuhl, and M. Braga, 2010, 3D inversion of airborne gravity gradiometry for iron ore exploration in Brazil: 80th Annual International Meeting, SEG, Expanded Abstracts, 1753–1757.
- Medeiros, W. E., and J. B. C. Silva, 1995, Gravity source moment inversion: A versatile approach to characterize position and 3D orientation of anomalous bodies: *Geophysics*, **60**, 1342–1353, doi: [10.1190/1.1836815](https://doi.org/10.1190/1.1836815).
- Menke, W., 1989, *Geophysical data analysis: Discrete inverse theory*: Academic Press Inc.
- Nagihara, S., and S. A. Hall, 2001, Three-dimensional gravity inversion using simulated annealing: Constraints on the diapiric roots of allochthonous salt structures: *Geophysics*, **66**, 1438–1449, doi: [10.1190/1.1487089](https://doi.org/10.1190/1.1487089).
- Nagy, D., G. Papp, and J. Benedek, 2000, The gravitational potential and its derivatives for the prism: *Journal of Geodesy*, **74**, 552–560, doi: [10.1007/s001900000116](https://doi.org/10.1007/s001900000116).
- Pedersen, L. B., and T. M. Rasmussen, 1990, The gradient tensor of potential field anomalies: Some implications on data collection and data processing of maps: *Geophysics*, **55**, 1558–1566, doi: [10.1190/1.1442807](https://doi.org/10.1190/1.1442807).
- Pilkington, M., 1997, 3D magnetic imaging using conjugate gradients: *Geophysics*, **62**, 1132–1142, doi: [10.1190/1.1444214](https://doi.org/10.1190/1.1444214).
- Portniaguine, O., and M. S. Zhdanov, 1999, Focusing geophysical inversion images: *Geophysics*, **64**, 874–887, doi: [10.1190/1.1444596](https://doi.org/10.1190/1.1444596).
- Portniaguine, O., and M. S. Zhdanov, 2002, 3D magnetic inversion with data compression and image focusing: *Geophysics*, **67**, 1532–1541, doi: [10.1190/1.1512749](https://doi.org/10.1190/1.1512749).
- Ramachandran, P., and G. Varoquaux, 2011, Mayavi: 3D visualization of scientific data: *Computing in Science & Engineering*, **13**, 40–50, doi: [10.1109/MCSE.2011.35](https://doi.org/10.1109/MCSE.2011.35).
- René, R. M., 1986, Gravity inversion using open, reject, and “shape-of-anomaly” fill criteria: *Geophysics*, **51**, 988–994, doi: [10.1190/1.1442157](https://doi.org/10.1190/1.1442157).
- Routh, P. S., G. J. Jorgensen, and J. L. Kisabeth, 2001, Base of the salt imaging using gravity and tensor gravity data: 71st Annual International Meeting, SEG, Expanded Abstracts, 1482–1484.
- Silva, J.B.C., and V.C.F. Barbosa, 2006, Interactive gravity inversion: *Geophysics*, **71**, no. 1, J1–J9, doi: [10.1190/1.2168010](https://doi.org/10.1190/1.2168010).
- Silva, J. B. C., and A. O. Cutrim, 1989, A robust maximum likelihood method for gravity and magnetic interpretation: *Geoexploration*, **26**, 1–31, doi: [10.1016/0016-7142\(89\)90017-3](https://doi.org/10.1016/0016-7142(89)90017-3).
- Silva, J.B.C., and G. W. Holmann, 1983, Nonlinear magnetic inversion using a random search method: *Geophysics*, **48**, 1645–1658, doi: [10.1190/1.1441445](https://doi.org/10.1190/1.1441445).
- Silva Dias, F.J.S., V.C.F. Barbosa, and J.B.C. Silva, 2007, 2D gravity inversion of a complex interface in the presence of interfering sources: *Geophysics*, **72**, no. 2, I13–I22, doi: [10.1190/1.2424545](https://doi.org/10.1190/1.2424545).
- Silva Dias, F.J.S., V.C.F. Barbosa, and J.B.C. Silva, 2009, 3D gravity inversion through an adaptive-learning procedure: *Geophysics*, **74**, no. 3, I9–I21, doi: [10.1190/1.3092775](https://doi.org/10.1190/1.3092775).
- Silva Dias, F.J.S., V.C.F. Barbosa, and J.B.C. Silva, 2011, Adaptive learning 3D gravity inversion for salt-body imaging: *Geophysics*, **76**, no. 3, I49–I57, doi: [10.1190/1.3555078](https://doi.org/10.1190/1.3555078).
- Tarantola, A., 2005, *Inverse problem theory and methods for model parameter estimation*: SIAM.
- Uieda, L., and V.C.F. Barbosa, 2012a, Animation of growth iterations during 3D gravity gradient inversion by planting anomalous densities: Figshare, <http://hdl.handle.net/10779/2f26602b43f73723987b8d04946bfa41>, accessed 25 April 2012.
- Uieda, L., and V.C.F. Barbosa, 2012b, Supplementary material to “Robust 3D gravity gradient inversion by planting anomalous densities” by L. Uieda and V. C. F. Barbosa: Figshare, <http://hdl.handle.net/10779/cbf817e4cc9ac3cf54bee7c649de1d3>, accessed 25 April 2012.
- Vasco, D. W., 1989, Resolution and variance operators of gravity and gravity gradiometry: *Geophysics*, **54**, 889–899, doi: [10.1190/1.1442717](https://doi.org/10.1190/1.1442717).
- Wilson, G. A., M. Cuma, and M. S. Zhdanov, 2011, Large-scale 3D inversion of airborne potential field data: 73rd Annual International Conference and Exhibition, EAGE, Extended Abstracts, K047.
- Zhdanov, M. S., R. G. Ellis, and S. Mukherjee, 2004, Regularized focusing inversion of 3D gravity tensor data: *Geophysics*, **69**, 925–937, doi: [10.1190/1.1778236](https://doi.org/10.1190/1.1778236).
- Zhdanov, M. S., A. Green, A. Gribenko, and M. Cuma, 2010a, Large-scale three-dimensional inversion of Earthscope MT data using the integral equation method: *Physics of the Earth and Planetary Interiors*, **8**, 27–35, doi: [10.1134/S1069351310080045](https://doi.org/10.1134/S1069351310080045).
- Zhdanov, M. S., X. Liu, and G. A. Wilson, 2010b, Rapid imaging of gravity gradiometry data using 2D potential field migration: 80th Annual International Meeting, SEG, Expanded Abstracts, 1132–1136.
- Zidarov, D., and Z. Zhelev, 1970, On obtaining a family of bodies with identical exterior fields — Method of bubbling: *Geophysical Prospecting*, **18**, 14–33, doi: [10.1111/gpr.1970.18.issue-1](https://doi.org/10.1111/gpr.1970.18.issue-1).